GE Energy

James C. Kinsey
Project Manager, ESBWR Licensing

PO Box 780 M/C J-70
Wilmington, NC 28402-0780
USA

T 910 675 5057
F 910 362 5057
jim.kinsey@ge.com

MFN 06-313
Supplement 1

Docket No. 52-010

April 16, 2007

U.S. Nuclear Regulatory Commission
Document Control Desk
Washington, D.C. 20555-0001

Subject: **Supplemental Response to Portion of NRC Request for Additional Information Letter No. 43 Related to ESBWR Design Certification Application - Supplement 1 and Supplement 2 Containment Fragility-RAI Number 19.2-58 S1 and 19.2-62 S1.**

Enclosure 1 contains GE's response to the subject NRC RAI transmitted via the Reference 1 questions and from the NRC Seismic Fragility Audit of February 5, 2007.

If you have any questions or require additional information regarding the information provided here, please contact me.

Sincerely,

Kathy Sedney for

James C. Kinsey
Project Manager, ESBWR Licensing

D068

Reference:

1. MFN 06-237, Letter from U.S. Nuclear Regulatory Commission to David Hinds, *Request for Additional Information Letter No. 43 Related to ESBWR Design Certification Application*, July 18, 2006..

2. MFN 06-313, *Response to Portion of NRC Request for Additional Information Letter No. 43 Related to ESBWR Design Certification Application –ESBWR Containment Fragility* –RAI Numbers 19.1-8 (b)(Revised Response), 19.1-9, 19.1-10, 19.1-16, 19.1-18, 19.2-4. 19.2-5,19.2-15, 19.2-16, 19.2-19, 19.2-20, 19.2-21, 19.2-23, 19.2-34, 19.2-58 through 19.2-62, and 19.2-64. September 12, 2006.

Enclosures:

1. MFN 06-313 Supplement 1, *Partial Response to RAI Letter No. 43 Related to ESBWR Design Certification Application (Previously Submitted Under MFN 06-313). -Containment Fragility- RAI Number 19.2-58 S1, and 19.2-62 S1.*

cc: AE Cubbage USNRC (with enclosures)
George Stramback GE/San Jose (with enclosures)
RE Brown GE/Wilmington (with enclosures)
EDRF Section 0000-0066-8978

ENCLOSURE 1

MFN 06-313 SUPPLEMENT 1

Partial Response to RAI Letter No. 43

Related to ESBWR Design Certification Application (Previously Submitted[1] Under MFN 06-313)

Containment Fragility- RAI Number 19.2-58 S1 and 19.2-62 S1

[1] Original response previously submitted under MFN 06-313. The previous response is included to provide historical continuity during review.

NRC RAI 19.2-58, Supplement 1

In PRA, Section 21.3.4.4, GE described an analysis to address the liner integrity for temperatures greater than 1000°K, using LS-DYNA3D. In the GE model, a piece of liner between a neighboring set of anchors and the presence of concrete behind the liner were considered. GE showed in Figures 21.3-22 that the resulting maximum effective plastic strains in the liner between anchors at temperatures 1400°K and 1650°K are 1.4% and 7.26%, respectively. In Section 21.3.4.3, GE stated that the drywell pressure is predicted to be around 6 bar (0.6Mpa). However, it is not obvious that the pressure load is included in the LS-DYNA 3D model. Provide:

a) the material models for both liner and concrete at high temperature used in LS-DYNA3D model, including stress-strain relation and strain rate effect.

b) a discussion of the effect of high temperature degradation on the ability of the liner and concrete to resist the pressure load.

GE Response:

First it should be noted that as stated in Section 21 of NEDO-33201 Rev 1, the code used is not the commercial version LS-DYNA3D but the LLNL code DYNA3D. This is a much advanced code, with unique capabilities in the areas of interest here, including explosive loads and/or high temperatures.

a) Material properties for the liner were provided in Figure 21.3.4.4.2 of Section 21 of NEDO-33201 Rev 1. Concrete properties are not relevant, as the time scale is way off the time scale needed to affect concrete wall structural stability.

b) The high internal pressures have no bearing on the concrete, which remains structurally intact. The liner, backed by the concrete, will deform under thermal stresses, and Section 21 of NEDO-33201 Rev 1 shows that this deformation is accommodated by creep, while remaining at strain levels well below what might be considered as potentially threatening.

NRC Assessment Following the February 5, 2007 Audit

Staff Assessment:

GE should provide a detailed description of material models used in the DYNA3D analysis described in Section 21 of NEDO-33201 Rev 1. It is not sufficient simply to identify it as "a much advanced code". As indicated in Figure 21.3.4.3-11 of Section 21 of NEDO-33201 Rev 1, the temperature profiles for both LDW and UDW could be very high. For Cases F and H, the upper drywell is subjected to temperature in excess to 1000° K for a long period of time. In a high temperature environment, load bearing capability of concrete degrades. GE should justify why the temperature of 1000° K or higher will not affect the concrete load bearing capability.

Audit Interest:

Discuss the concrete material model in DYNA3D that was used in the GE analysis. Also, discuss how GE considered the concrete load bearing capability for Cases F and H in Figure 21.3.4.3-11 of Section 21 of NEDO-33201 Rev 1.

Status Update/Resolution of RAI:

a) See 19.2-51.

b) In addition, GE will provide the reference material to DYNA3D concrete material model.

GE Response

a) See response to 19.2-51 Supplement 1. It is contained in Enclosure 1 to MFN 06-428 S2.

b) The paper describing the concrete model for DYNA3D is attached.

NRC RAI 19.2-62, Supplement 1

In PRA, Section 21.4.4.4, GE described the structural response analyses for the pedestal and the BiMAC device subjected to EVE pressure impulses. The K&C model (Karagozian and Case) was used for concrete and rebars included in the model. The pressure impulse loads analyzed range from 200 kPa-s to 600 kPa-s. The impulse loads are characterized as high frequency loads and, therefore, strain rate effect on material properties is expected to be important. Provide:

a) a description of how the strain rate effect is considered for both concrete and steel material models (material properties are typically obtained from pseudo static tests (low cyclic));

b) a detailed description of the K&C model;

c) a description of how the reinforced concrete pedestal is modeled in the LS-DYNA3D model;

d) a description of how the failure of the pedestal impacts the RPV supports, which are structurally supported by the pedestal.

GE Response:

a) and b) The model used is not the commercial LS-DYNA3D but LLNL's own code developed and verified for explosive loads, as described in reference "Noble, C. J. et al (2005). "Concrete Model Description and Summary of Benchmark Studies for Blast Effects and Simulation", UCRL-215024, Lawrence Livermore National Laboratory (July, 2005)" given in Section 21.4 of NEDO-33201 Rev 1. This reference contains all descriptions requested under a) and b).

c) This is already given in Section 21.5 of NEDO-33201 Rev 1 (Figures 21.5.4.4-2 and related text).

d) As noted already in Section 21.5 of NEDO-33201 Rev 1, SE loads on the pedestal are localized and any hypothesized failure would be local, having no impact on the pedestal as a whole, and reactor-bearing capacity.

Staff Assessment:

The issue is whether the K&C model includes strain rate effect, which is important in characterizing the concrete response to shock loads, and whether any test data was used to define the concrete strain-pressure relationship. GE should provide the reference or provide a detailed description of the concrete model in the reference. Further clarification is needed.

Audit Interest

Typical concrete properties are determined based on static tests (low cycle). However, for shock loads, strain rate effect needs to be considered in defining the concrete properties. Discuss how the K&C model includes strain rate effect in characterizing the concrete response to shock loads, and what data GE used to describe the strain rate effect in the concrete strain-pressure relationship.

Status Update/Resolution of RAI

GE will provide the reference material for the K&C model.

GE Response

Complete definition of the K&C model is now provided in a supplement to PRA Chapter 21 (UCRL-TR-227386). This reference was provided in response to RAI 19.2-60 in MFN 07-202.

Pergamon

Int. J. Impact Engng Vol. 19, Nos. 9–10, pp. 847–873, 1997

PII: S0734-743X(97)00023-7
0734-743X/97 $17.00 + 0.00

A PLASTICITY CONCRETE MATERIAL MODEL FOR DYNA3D

L. JAVIER MALVAR†, JOHN E. CRAWFORD†, JAMES W. WESEVICH† and DON SIMONS‡

† Karagozian & Case, 625 North Maryland Avenue, Glendale, CA 91206, U.S.A. and ‡ Logicon RDA, 6053 West Century Boulevard, Los Angeles, CA 90009, U.S.A.

(*Received* 24 *March* 1995; *in revised form* 16 *January* 1997)

Summary—Lagrangian finite element codes with explicit time integration are extensively used for the analysis of structures subjected to explosive loading. Within these codes, numerous material models have been implemented. However, the development of a realistic but efficient concrete material model has proven complex and challenging.

The plasticity concrete material model in the Lagrangian finite element code DYNA3D was assessed and enhanced. The main modifications include the implementation of a third, independent yield failure surface; removal of the tensile cutoff and extension of the plasticity model in tension; shift of the pressure cutoff; implementation of a three invariant formulation for the failure surfaces; determination of the triaxial extension to triaxial compression ratio as a function of pressure; shear modulus correction; and implementation of a radial path strain rate enhancement. These modifications insure that the response follows experimental observations for standard uniaxial, biaxial and triaxial tests in both tension and compression, as shown via single element analyses. The radial path strain rate enhancement insures constant enhancement for all those tests. As a full scale example, a standard dividing wall subjected to a blast load is analyzed and the effects of the modifications assessed. © 1997 Published by Elsevier Science Ltd.

NOTATION

a_{ij}	parameters defining the three-parameters failure surfaces
f'_c, f_t	compressive and tensile strength of concrete, respectively
G	shear modulus
I_1	$(\sigma_1 + \sigma_2 + \sigma_3)$ first invariant of stress tensor
J_2	$((s_1^2 + s_2^2 + s_3^2)/2)$ second invariant of the deviatoric stress tensor
J_3	$(s_1 s_2 s_3)$ third invariant of the deviatoric stress tensor
K	bulk modulus
p	pressure $(I_1/3)$
p_c	pressure cutoff in tension
r_c, r_t	radii of the compressive and tensile meridians, respectively
r_f	strain rate enhancement factor
Υ	$(\Delta\sigma = \sqrt{3J_2})$ failure surface for the deviatoric stresses
$\Delta\sigma$	$(\sqrt{3J_2})$ failure surface for the deviatoric stresses
λ	modified effective plastic strain (damage parameter)
η	parameter indicating the relative location of the current failure surface
ψ	ratio of tensile to compressive meridian radii at a given pressure
φ	scaling factor

1. INTRODUCTION

In the analysis of complex structures subjected to blast loading and large deformations, Lagrangian finite element codes with explicit time integration have become a necessary and efficient tool [1–4]. In these codes a limited element library including trusses, beams, shells and solids has proven sufficient. However, extensive material libraries have been required for representation of the vast range of material behaviors. In the case of reinforced concrete structures, implementation of a realistic but efficient concrete material model has proven complex and challenging.

Numerous analyses for prediction of small and full scale blast tests of reinforced concrete structures sponsored by the Defense Special Weapons Agency (formerly the Defense Nuclear Agency) have provided an opportunity to revisit the existing material models in the finite element code DYNA3D [1]. The models potentially suitable for representing the

concrete's constitutive behavior were assessed over the full range from elastic response to failure. The most robust one, material model 16, still contains several shortcomings. In this report those deficiencies and the corresponding corrections are described.

ORIGINAL MATERIAL MODEL

The Lagrangian finite element code DYNA3D was originally developed by the Lawrence Livermore National Laboratory (LLNL) [1]. Within DYNA3D, several material models have been used in the past to represent concrete, namely, material models 5 (Soil and Crushable Foam), 16 (Concrete/Geological Material), 17 (Isotropic Elastic–Plastic with Oriented Cracks), 25 (Extended Two Invariant Geologic Cap). Materials 5, 17 and 25 have exhibited significant limitations in modeling concrete behavior [5]. Material model 16, however, appeared more appropriate and presented some attractive features which could be easily enhanced.

Overview

The original material model 16 (subroutine f3dm16.f) decouples the volumetric and deviatoric responses. An equation of state gives the current pressure as a function of current and previous minimum (most compressive) volumetric strain. Once the pressure is known, a moveable surface—herein denominated a *yield* or *failure* surface—limits the second invariant of the deviatoric stress tensor. The volumetric response is easily captured via a tabulated input such as the one in equation of state 8. No changes were deemed necessary for this part of the response. However, the deviatoric response (in f3dm16.f) did present some shortcomings which were addressed with modifications to be described in detail later. Due to the decoupling of volumetric and deviatoric responses, this model has the limitation of not incorporating shear dilation which is observed with concrete. For the case of significant structural lateral restraints and low damage levels this will result in responses softer than expected. During initial loading or reloading, the deviatoric stresses remain elastic until the stress point reaches the initial yield surface. The deviatoric stresses can then increase further until the maximum yield surface is reached. Beyond this stage the response can be perfectly plastic or soften to the residual yield surface (see Fig. 1). Whenever the stress point is on the yield surface and the stress increment corresponds to loading on that surface, plastic flow occurs in accordance with a Prandtl-Reuss (volume preserving) flow rule, implemented by the well known "radial return" algorithm. The model also incorporates a tensile cutoff and a pressure cutoff, which are detailed in the following.

Original deviatoric response

Stress limits. The function $\Delta\sigma$ which limits the deviatoric stresses is defined as a linear combination of two fixed three-parameter functions of pressure:

$$\Delta\sigma = \eta\Delta\sigma_m + (1-\eta)\Delta\sigma_r,$$

where

$$\Delta\sigma_m = a_0 + \frac{p}{a_1 + a_2 p} \quad \text{(maximum stress difference)},$$

$$\Delta\sigma_r = a_{0f} + \frac{p}{a_{1_f} + a_2 p} \quad \text{(residual stress difference)},$$

and where $p = -(\sigma_{xx} + \sigma_{yy} + \sigma_{xx})/3$ is the pressure (stresses are positive in tension, pressure is positive in compression). The parameter η is a user-defined function of a modified effective plastic strain measure λ. The function $\eta(\lambda)$ is intended to first increase from some initial value up to unity, then decrease to zero representing softening. Hence, one may

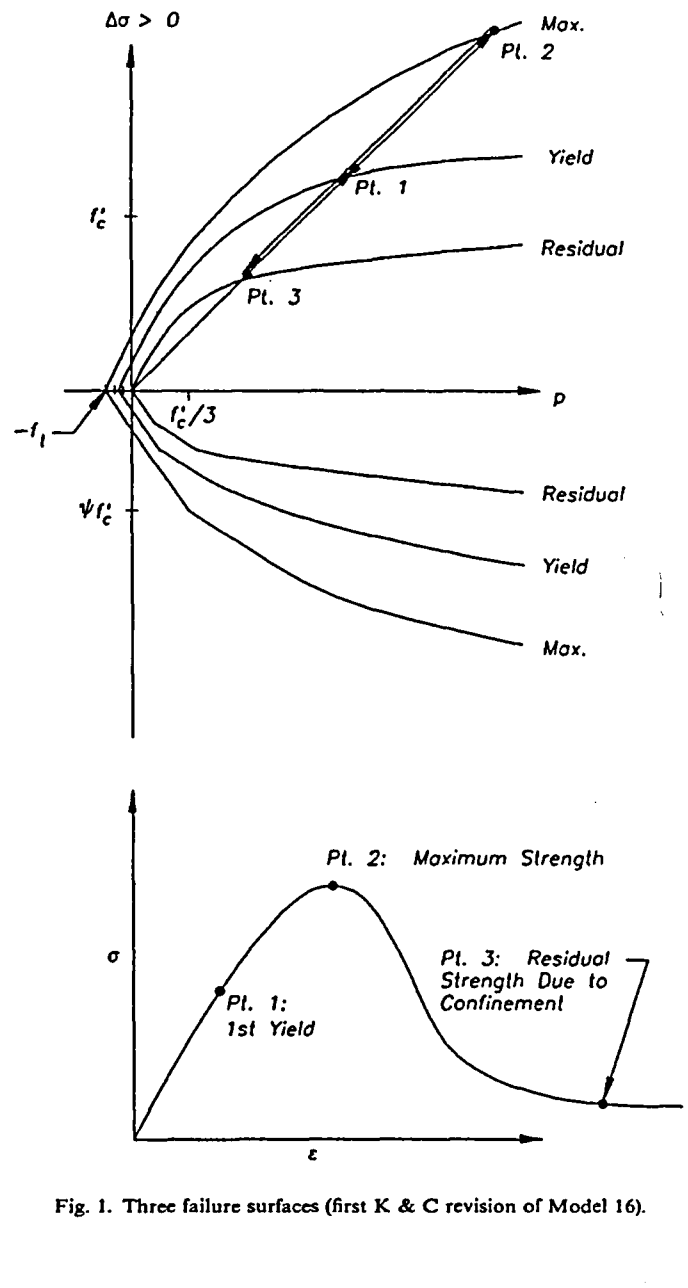

Fig. 1. Three failure surfaces (first K & C revision of Model 16).

think of the yield surface as migrating between $\Delta\sigma_r$, representing the minimum or residual strength, and $\Delta\sigma_m$, the maximum strength. The initial yield surface is given by

$$\Delta\sigma_y = \eta_y \Delta\sigma_m + (1 - \eta_y)\Delta\sigma_r$$

where $\eta_y = \eta(0)$ is the initial value of η before any plasticity has occurred. The DYNA3D manual includes a suggestion (at the end of its section on material model 16) which specifies a value $\eta_y = 0.309$.

Available triaxial compression concrete data indicate that, for the initial yield surface, the principal stress difference $\Delta\sigma_y$ should be about 45% of the maximum stress difference [6]. On the other hand, the residual strength should vanish for the unconfined compression test. Furthermore, because the two fixed surfaces become parallel for large values of p, they cannot properly represent the brittle–ductile transition point. The original formulation, with the constraint that the initial, maximum, and residual yield surfaces be linearly related, therefore cannot properly capture the experimental data. This suggests the need for a third fixed yield surface independent from the other two.

Compressive meridian. Data for the compressive meridian are usually obtained from an unconfined compression test and triaxial compression tests with various levels of confinement [6, 7]. For the original model 16, a minimum of two nonzero levels of confinement are needed since three parameters define the compressive meridian. The usual tests provide no data for pressures below $f'_c/3$ (failure in an unconfined compression test). The three-parameter maximum failure surface just described will usually overestimate the strength when extrapolated to pressures below $f'_c/3$. Similarly, this formulation would overestimate the principal stress difference for the biaxial tension test.

Tensile meridian. It is well known that the tensile or extension meridian of the failure surface for concrete is usually lower (closer to the hydrostat at the same pressure) than the compressive meridian, e.g. see Section 5 of [7]. Experimental data suggest that the ratio of the tensile to compressive meridian, herein denoted ψ, varies from about 0.5 at negative (tensile) pressures to unity at high confinements. Using equal meridians at low pressures will yield erroneous results (see Fig. 2).

Tensile cutoff. In an attempt to alleviate the previously noted shortcoming at low pressures, the original material model incorporates at tensile cutoff which limits the maximum principal stress to the tensile strength f_t (see Fig. 2). For intermediate pressures ($0 < p < f'_c/3$) this does not solve the problem. In addition the tensile cutoff algorithm reduces the current stress state to zero in 20 steps. This arbitrary and abrupt stress decrease contrasts with the smooth decay offered by the plasticity model when transitioning between the maximum and residual failure surfaces.

Pressure cutoff. The original model also incorporates a pressure cutoff which prevents the pressure from going below $f_t/3$ (see Fig. 2). Although this does not affect the uniaxial tensile test, it does limit the principal stress difference to $f_t/2$ for a biaxial tensile test, and to

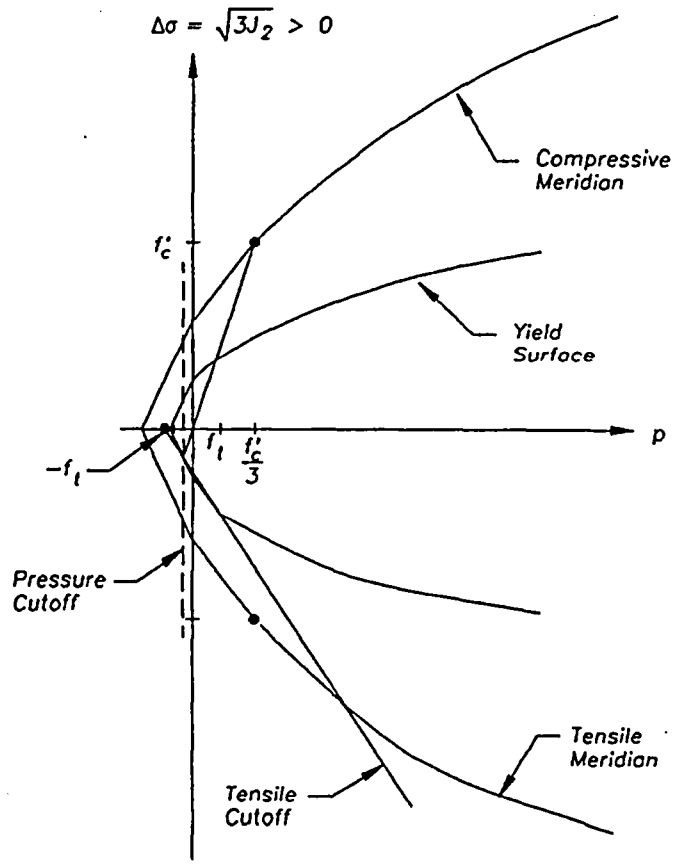

Fig. 2. Original LLNL-DYNA3D failure surfaces.

$f_t/3$ for a triaxial tensile test. These limits disagree with experimental data showing that in both cases the principal stress difference should reach approximately f_t [7–9]. In addition, whenever the pressure cutoff is reached in the original model, the current state of stress is maintained and no stress decay takes place upon further straining.

Rate enhancement. In the original model, at any given *pressure*, the failure surfaces are expanded by a rate enhancement factor which depends on the effective deviatoric strain rate, as shown in Fig. 3. Enhancing strength at a given pressure is inconvenient, because the rate enhancement factors available in the literature apply to the uniaxial unconfined compression and extension paths, not to a pure shear path. It is possible to derive the following formula to relate the test data to the input data in compression:

$$r_c = \frac{3a_1 f'_c r_f + a_2 f'^2_c r_f^2}{3a_0 a_1 + (1 + a_0 a_2) f'_c r_f},$$

where r_c = input to DYNA3D (rate enhancement factor at fixed pressure), r_f = experimental rate enhancement factor from an unconfined uniaxial compression test, f'_c = compressive strength, and a_i = parameters defining the maximum stress difference $\Delta\sigma_m$. However, the original program uses the same factor for enhancing stress states at negative pressures. When calibrated to unconfined compression, it can be shown that this results in almost no enhancement in the uniaxial tension test.

Elastic behavior. The original LLNL material model 16 has two options for the elastic response, both isotropic. Both use the bulk modulus from the pressure-volume relation to compute a second elastic constant. One assumes a constant Poisson's ratio, the other a constant shear modulus. Although a constant shear modulus absolutely guarantees that no elastic energy can be generated, that option was dropped in favor of the second option, in which the user specifies a value of Poisson's ratio. When used with equation of state 8, the model derives a shear modulus from the current *unloading* bulk modulus. This method

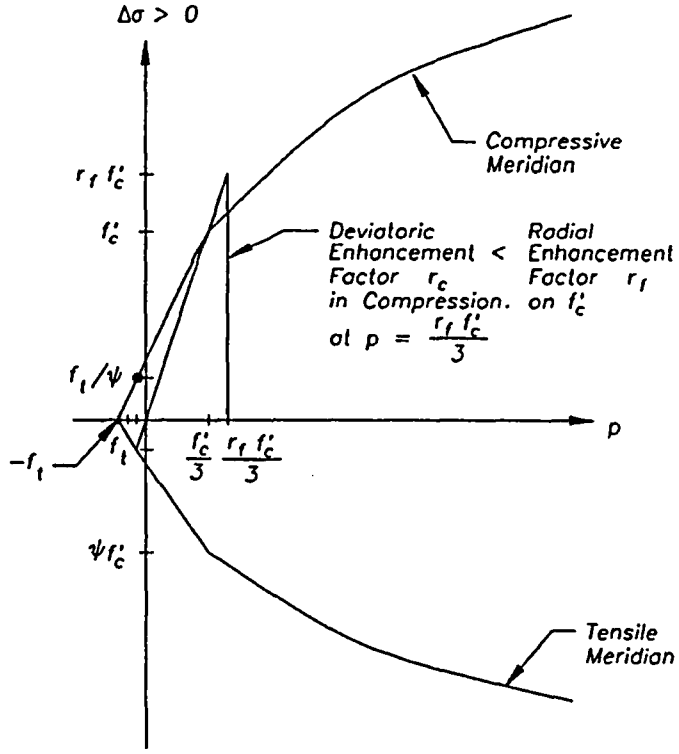

Fig. 3. Original LLNL-DYNA3D rate enhancement in compression.

easily leads to inconsistencies such as negative Poisson ratios upon initial loading [10]. The assumption of constant Poisson's ratio was retained, but the computation of the shear modulus was modified as described later.

NEW MATERIAL MODEL

The original material model 16 has been significantly modified to correct most of the shortcomings noted in the previous section.

New pressure cutoff

The pressure cutoff p_c now has an initial value of $-f_t$ (see Fig. 4). Together with changes in the maximum failure surface described below, both the biaxial and triaxial tensile tests can now reach a principal stress difference of f_t. Upon failure in the negative pressure range, the parameter η is used not only to reduce the current failure surface from the maximum to the residual, but also to increase the pressure cutoff from $-f_t$ to zero in a smooth fashion. This is done by checking the pressure returned by the equation of state subroutine, and resetting it to p_c if it violates $p \geq p_c$, where

$$p_c = \begin{cases} -f_t & \text{if the maximum failure surface has not been reached (hardening),} \\ -\eta f_t & \text{if the maximum failure surface has been reached (softening).} \end{cases}$$

Note that although implemented in the concrete material model subroutine, this modification can override the pressure calculated in the equation of state. This pressure cutoff is necessary as otherwise the equation of state would calculate very large negative pressures for large volumetric extensions beyond cracking, which would be physically incorrect.

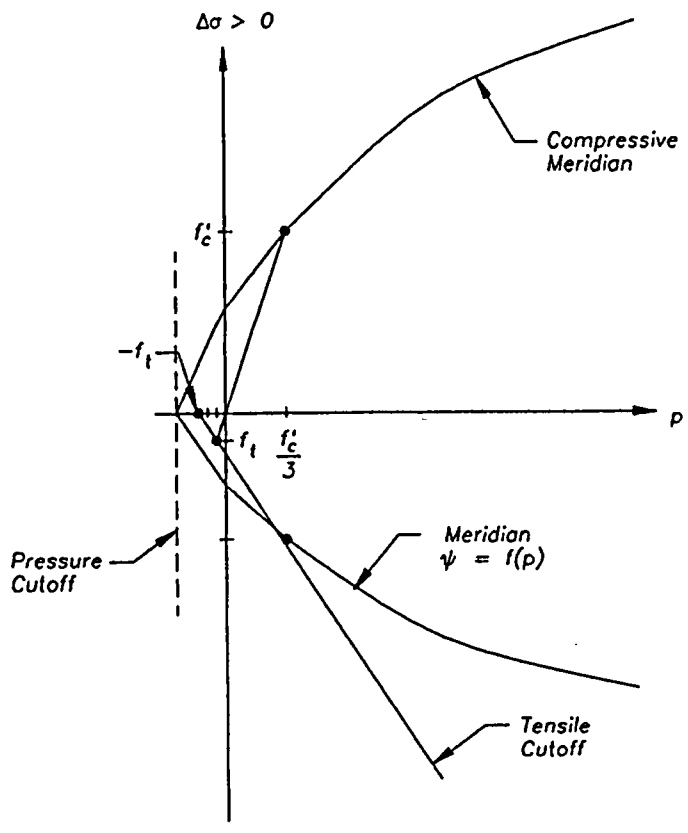

Fig. 4. Willam Warnke failure surface.

Compressive meridians of the fixed failure surfaces

New fixed surface to represent initial yielding. A third, independent, fixed surface has been implemented with three new parameters (a_{0y}, a_{1y}, a_{2y}). This surface represents initial yielding and is given by

$$\Delta\sigma_y = a_{0y} + \frac{p}{a_{1y} + a_{2y}p}.$$

In addition, since for concrete the residual strength in tension is zero, the pressure independent parameter in the formulation of the residual surface is not needed, i.e., $a_{0f} = 0$. To permit the residual and the maximum failure surfaces to intersect at a point representing the brittle–ductile transition, a new parameter a_{2f} has been added. The residual surface now takes the form

$$\Delta\sigma_r = \frac{p}{a_{1f} + a_{2f}p}.$$

In the new model, after reaching the initial yield surface but before the maximum failure surface, the current surface is obtained as a linear interpolation between the two:

$$\Delta\sigma = \eta(\Delta\sigma_m - \Delta\sigma_y) + \Delta\sigma_y,$$

where η varies from 0 to 1 depending on the accumulated effective plastic strain parameter λ. After reaching the maximum surface the current failure surface is similarly interpolated between the maximum and the residual:

$$\Delta\sigma = \eta(\Delta\sigma_m - \Delta\sigma_r) + \Delta\sigma_r.$$

The function $\eta(\lambda)$ is input by the user as a series of (η, λ) pairs. This function would normally begin at 0 at $\lambda = 0$, increase to 1 at some value $\lambda = \lambda_m$, and then decrease to 0 at some larger value of λ. Since λ is non-decreasing, this would permit $\Delta\sigma$ sequentially to take on the values $\Delta\sigma_y, \Delta\sigma_m$, and $\Delta\sigma_r$. In fact, there are no internal checks to guarantee that the user's input takes on these specific values. Thus, at the beginning of the subroutine the value of λ_m is defined simply as the value of λ corresponding to the first relative maximum of η in the input table. Then, whenever $\lambda \le \lambda_m$ the current surface in interpolated between the initial yield and the maximum; conversely, if $\lambda > \lambda_m$ the current surface is interpolated between the maximum and the residual.

In summary a total eight parameters define the three fixed surfaces, as follows:

$$\Delta\sigma_m = a_0 + \frac{p}{a_1 + a_2 p} \quad \text{(maximum failure surface)},$$

$$\Delta\sigma_r = \frac{p}{a_{1f} + a_{2f}p} \quad \text{(residual failure surface)},$$

$$\Delta\sigma_y = a_{0y} + \frac{p}{a_{1y} + a_{2y}p} \quad \text{(yield failure surface)}.$$

At pressures above the brittle–ductile transition, $\Delta\sigma_r$ should be limited to $\Delta\sigma_m$. In the code this is ensured by resetting $\Delta\sigma_r$ to $\Delta\sigma_m(p)$ if $\Delta\sigma_r$ from the nominal formula exceeds $\Delta\sigma_m(p)$. The yield surface is similarly limited to $\Delta\sigma_m$.

Determination of maximum failure surface parameters. The parameters (a_0, a_1, a_2) should be determined from laboratory data in unconfined compression tests and conventional triaxial compression tests at a range of confining pressures. With only three data points, an exact fit can easily be made. With more than three, some sort of least-squares method could be employed. Alternatively, estimates for the values of these parameters can be obtained as follows:

- The parameter a_0 represents the intersection of the maximum failure surface with the stress difference axis, i.e. $\Delta\sigma|_{p=0} = a_0$.

- Parameter a_1 is the inverse of the slope at $p = 0$, i.e.

$$\left[\frac{\mathrm{d}}{\mathrm{d}p}\Delta\sigma\right]_{p=0} = \frac{1}{a_1}.$$

- For very large values of p, the denominator on the right-hand side of the equation is dominated by the term $a_2 p$ (the term a_1 becomes relatively insignificant). Hence

$$\Delta\sigma - a_0 \to \frac{1}{a_2} \quad \text{as} \quad p \to \infty.$$

Determination of initial yield surface parameters. To define the initial yield surface, (a_{0y}, a_{1y}, a_{2y}) have to be determined. Available data [6] suggest that this surface is approximately the locus of points at $\Delta\sigma = 0.45\Delta\sigma_m$ on triaxial compression paths, as shown in Fig. 5. For a point $(p, \Delta\sigma_m)$ on the maximum failure surface, the corresponding point $(p', \Delta\sigma_y)$ on the yield surface is

$$\Delta\sigma_y = 0.45\Delta\sigma_m \quad \text{and} \quad p' = p - \frac{0.55}{3}\Delta\sigma_m.$$

From the latter equation, p can be obtained as a function of p':

$$p = -\frac{1}{2}\left[\frac{a_1}{a_2} - p' - \frac{0.55}{3}\left(a_0 + \frac{1}{a_2}\right)\right] - \frac{1}{2}\sqrt{\left[\frac{a_1}{a_2} - p' - \frac{0.55}{3}\left(a_0 + \frac{1}{a_2}\right)\right]^2 + 4\left(\frac{0.55 a_0 a_1}{3a_2} + \frac{a_1}{a_2}p'\right)},$$

while the former equation gives $\Delta\sigma_y$ as a function of p:

$$\Delta\sigma_y = 0.45\left(a_0 + \frac{p}{a_1 + a_2 p}\right),$$

enabling $\Delta\sigma_y$ to be computed as a function of p'. A plot of $\Delta\sigma_y$ is included in Fig. 5 for SAC5 material properties [11].

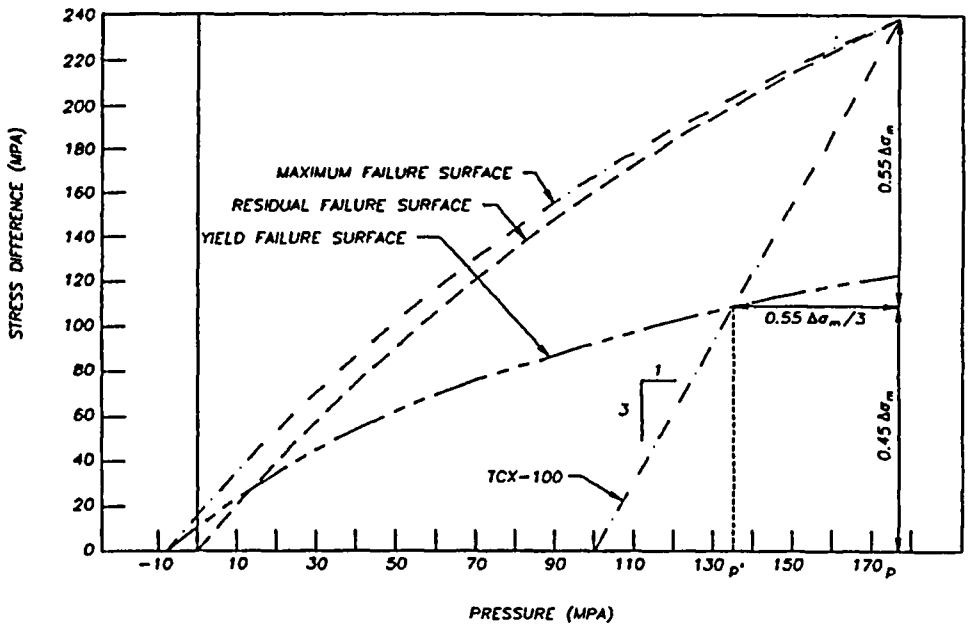

Fig. 5. Yield surface determination from triaxial compression tests.

Since the proposed formulation has three parameters, the curve $\Delta\sigma_y(p')$ can be approximated by choosing three points from the curve and solving for the parameters (a_{0y}, a_{1y}, a_{2y}). By picking the first point at $p' = 0$, which gives $(\Delta\sigma_y = a_{0y})$, only two equations with two unknowns have to be solved for a_{1y} and a_{2y}.

Scaling of failure surfaces. If a new concrete with known unconfined compression strength $f'_{c,new}$ is to be modeled, but its failure surfaces are otherwise unknown, then one way of scaling data from a known material is as follows:

$$\text{Define} \quad r = \frac{f'_{c,new}}{f'_{c,old}},$$

where $f'_{c,old}$ is the unconfined compressive strength in a previously modelled concrete. Then the new material failure surfaces can be taken as

$$\Delta\sigma_n = a_{0n} + \frac{p}{a_{1n} + a_{2n}p}$$

with the new coefficients (a_{0y}, a_{1y}, a_{2y}) written in terms of the old ones as

$$a_{0n} = a_0 r, \quad a_{1n} = a_1, \quad a_{2n} = a_2/r.$$

Damage accumulation

New shear damage accumulation. The current failure surface is interpolated from the maximum failure surface and either the yield or the residual failure surface as

$$\Delta\sigma = \eta(\Delta\sigma_m - \Delta\sigma_{min}) + \Delta\sigma_{min},$$

where $\Delta\sigma_{min}$ is either $\Delta\sigma_y$ or $\Delta\sigma_r$ depending on whether $\lambda \le \lambda_m$ or $\lambda > \lambda_m$, and where η is a function of λ. In the original LLNL model 16, the modified effective plastic strain λ, is defined as

$$\lambda = \int_0^{\bar{\varepsilon}^p} \frac{d\bar{\varepsilon}^p}{(1 + p/f_t)^{b_1}},$$

where the effective plastic strain increment is given by $d\bar{\varepsilon}^p = \sqrt{(2/3)\varepsilon^p_{ij}\varepsilon^p_{ij}}$.

In the new model, two changes have been implemented. First rate effects were included, and second, the parameter b_1 is replaced by b_2 for tensile pressure $(p < 0)$, as follows:

$$\lambda = \begin{cases} \displaystyle\int_0^{\bar{\varepsilon}^p} \frac{d\bar{\varepsilon}^p}{r_t(1 + p/r_t f_t)^{b_1}} & \text{for } p \ge 0, \\ \displaystyle\int_0^{\bar{\varepsilon}^p} \frac{d\bar{\varepsilon}^p}{r_t(1 + p/r_t f_t)^{b_2}} & \text{for } p < 0. \end{cases}$$

Note that at $p = 0$, the denominator is a continuous function. In this way, the damage evolution can be different in tension and compression, if needed.

Volumetric damage. With damage accumulation as just described, if a triaxial tensile test is modelled, wherein the pressure decreases from 0 to $-f_t$ with no deviators, then no damage accumulation occurs. The parameter λ remains 0 and so does η. The equation of state decreases the pressure to $-f_t$ but keeps it at that level thereafter. To implement a pressure decay after tensile failure, a volumetric damage increment can be added to the deviatoric damage whenever the stress path is "close" to the triaxial tensile test path, i.e. the negative hydrostatic axis. The closeness to this path is measured by the ratio $|\sqrt{3J_2}/p|$, which, for example, is 1.5 for the biaxial tensile test. To limit the effects of this change to the

paths close to the triaxial tensile path, the incremental damage is multiplied by a factor f_d given by

$$f_d = \begin{cases} 1 - \dfrac{|\sqrt{3J_2}/p|}{0.1}, & 0 \le |\sqrt{3J_2}/p| < 0.1, \\ 0, & |\sqrt{3J_2}/p| \ge 0.1. \end{cases}$$

The modified effective plastic strain is incremented by

$$\Delta\lambda = b_3 f_d k_d (\varepsilon_v - \varepsilon_{v,\text{yield}})$$

where b_3 is the input scalar multiplier, k_d the internal scalar multiplier, ε_v the volumetric strain, and $\varepsilon_{v,\text{yield}}$ the volumetric strain at yield.

Determination of damage evolution parameters b_2, b_3 and b_1. The values of b_2 and b_3 govern the softening part of the unconfined uniaxial tension stress–strain curve as the stress point moves from the maximum to the residual failure surfaces. It is well known that, unless such softening is governed by a localization limiter or characteristic length, the results will not be objective upon mesh refinement, i.e. they will be mesh-dependent [12]. One way to eliminate this mesh dependency is to force the area under the stress-strain curve to be G_f/h, where G_f is the fracture energy and h the element size. If the localization occurs in one element, $h = w_c$ where w_c is the crack front width or localization width, and typically w_c is 1–6 times the maximum aggregate size [12]. The fracture energy usually varies from 40 to 175 N/m (0.23 to 1 lbf/in) according to the European CEB-FIP model code (Section 2.1.3.3.2: Fracture Energy) [9]. This smeared Crack Band model insures mesh size independence [12, 13]. However, there may still be some effects of mesh topology on crack direction both in statics and dynamics [12, 14].

In a typical analysis, a localization width (width of the localization path transverse to the crack advance, e.g. one element width, or cube root of the element volume in 3D) is chosen together with G_f. The parameter b_2 is determined by iterative calculations until the area under the stress–strain curve for a uniaxial unconfined tensile test coincides with G_f/h. Similarly b_3 is found using a hydrostatic triaxial tensile test. An example of the effects of b_2 and b_3 on the stress–strain response of a single element subjected to uniaxial and triaxial tensile tests is shown in Fig. 6. If the analysis yields a different localization width than

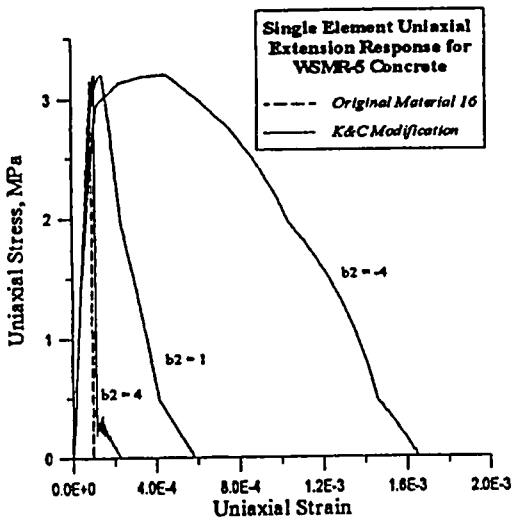

(a) Parameter b_2: effect on uniaxial tension strain softening.

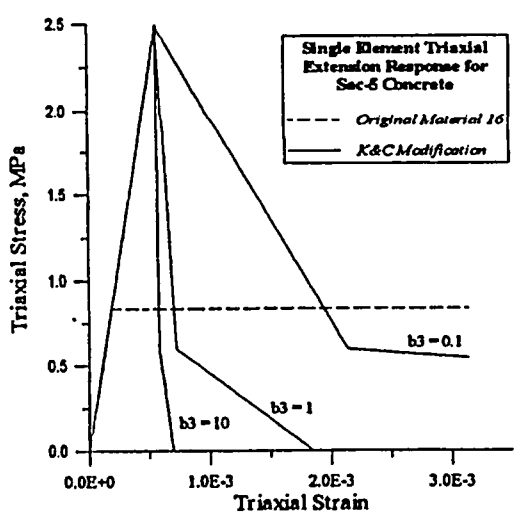

(b) Parameter b_3: effect on triaxial tensile strain softening.

Fig. 6. Effects of parameters b_2 and b_3 on tension softening. (a) Parameter b_2: effect on uniaxial tension strain softening. (b) Parameter b_3: effect on triaxial tensile strain softening.

anticipated, this should be corrected and the calculation restarted. These parameters will be of importance when the structure analyzed is lightly reinforced or is tension- or shear-critical. In dynamic analyses the localization pattern may vary during the run, depending on the relative amount of damping.

Similar considerations should be brought to bear when selecting a value for b_1, which governs softening in compression. The parameter b_1 is used to match observed compression behavior at various levels of transverse confinement. Figure 7 shows the ability of the model to reproduce test data from [6] for an unconfined compression test, as well as for four more levels of confinement. In this example, the 4-in. tall, 2-in. diameter cylinders were modeled using single elements.

Material model assessment for monotonic load paths. Figure 6(a) shows a comparison between the original and the new model for an unconfined uniaxial tension test. It is observed that the original model is almost perfectly brittle and cannot represent softening, whereas the new one can capture various softening patterns depending upon the given fracture energy (assumed a material constant) and the element size. The energy dissipated in the tension softening stage can be significant in cases of tensile or shear failure.

Figure 6(b) shows a comparison between original and new model for a hydrostatic tensile test. It is observed that the original model reaches one-third of the tensile strength, then remains at that stress level upon further straining, thus dissipating unrealistic amounts of energy. Similarly, if a biaxial tension test is represented, the old model reaches (and remains at) a stress of one-half the tensile strength. Note that in Fig. 6(b) only a few points were used to model the stress–strain curve. Figure 7 shows the model capability to represent triaxial compression tests on cylinders using single elements, and including the unconfined uniaxial compression test. Figure 8 shows the ability of the model to capture the actual biaxial compressive strength. The biaxial strength should be around 1.15 times the unconfined uniaxial compressive strength according to Kupfer *et al.* [8]. The biaxial compression loading path is initially parallel to the tensile meridian and is very sensitive to the choice of a two versus three invariant formulation (addressed in the next section). This explains why the original two-invariant model yields a grossly inaccurate biaxial compressive strength of about 5 times the unconfined uniaxial compressive strength.

In summary, the model is able to capture proper material behavior in uniaxial, biaxial, and triaxial monotonic tension and compression. After tensile fracture, the model will still be able to carry deviatoric stresses as long as the pressure becomes positive (compressive). In this case, the stress state will be located on a surface close to, or coincident with, the residual failure surface, depending on the amount of damage incurred.

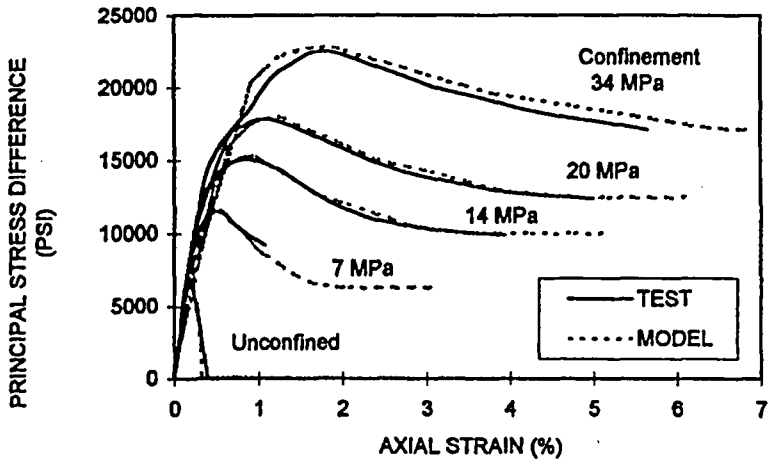

Fig. 7. Model representation of triaxial compression tests.

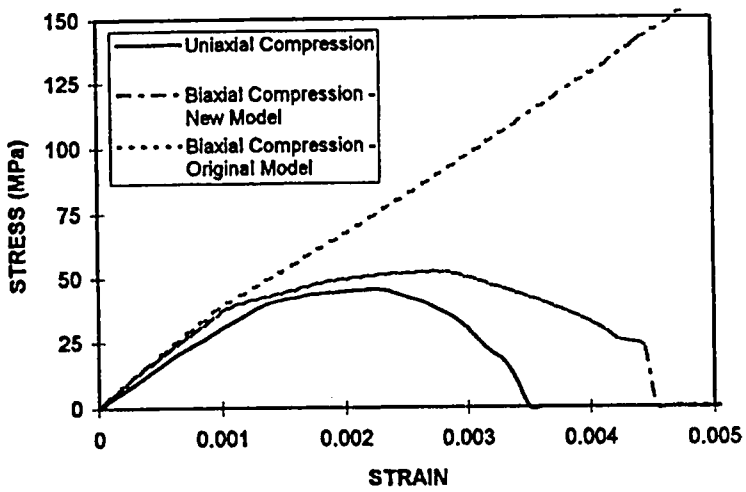

Fig. 8. Biaxial compression test.

Three-invariant failure surface formulation

Development of a three-invariant model. The previous $\Delta\sigma$ versus p relationships actually define only the compressive meridians of the failure surfaces in principal stress space. The original material model 16 assumes the full failure surfaces are obtained by rotating these meridians around the hydrostatic axis, thereby forming circular cross sections in the deviatoric planes. The surfaces are functions of pressure and the second invariant of the deviatoric stress tensor, J_2, whose square root is proportional to the radius of the circle. A third invariant, such as J_3 or Lode angle θ (angular offset in the deviatoric plane of the stress point from the image of a positive [tensile] principal stress axis) may be introduced to permit more general shapes in the deviatoric plane, such as the triangular curves with smooth corners shown in Fig. 9(a). For concrete the deviatoric section typically transitions from this shape at low pressures to circular at high pressures. Figures 9(b) and 9(c) show the large difference that can exist between the tensile and compressive meridians. Moreover, the difference is amplified when considering failure levels under compressive, proportional loadings, represented by rays emanating from the origin in stress space. These differences can be captured in the model only if a third invariant is included.

To introduce the third invariant, a dependence on the Lode angle θ [Fig. 10(a)] is sought. The shape proposed by Willam and Warnke [7] is adopted, providing a smooth, convex triangular surface generated by elliptical segments as shown in Fig. 10(b). If r_c is the distance from the hydrostatic axis to the failure surface at the compressive meridian, and r_t the distance at the tensile meridian, then at any intermediate position the distance r ($r_t < r < r_c$) will be given by

$$r = \frac{2r_c(r_c^2 - r_t^2)\cos\theta + r_c(2r_t - r_c)\sqrt{4(r_c^2 - r_t^2)\cos^2\theta + 5r_t^2 - 4r_t r_c}}{4(r_c^2 - r_t^2)\cos^2\theta + (r_c - 2r_t)^2}.$$

By dividing both sides by r_c, then dividing the numerator and denominator of the right-hand side by r_c^2, we obtain

$$r' = \frac{2(1 - \psi^2)\cos\theta + (2\psi - 1)\sqrt{4(1 - \psi^2)\cos^2\theta + 5\psi^2 - 4\psi}}{4(1 - \psi^2)\cos^2\theta + (1 - 2\psi)^2},$$

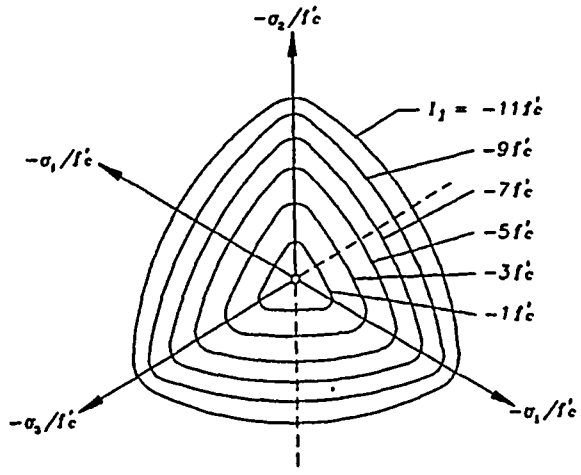

(a) Deviatoric sections for increasing pressure.

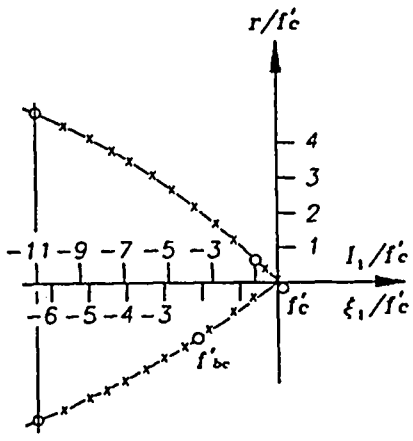

(b) Hydrostatic section.

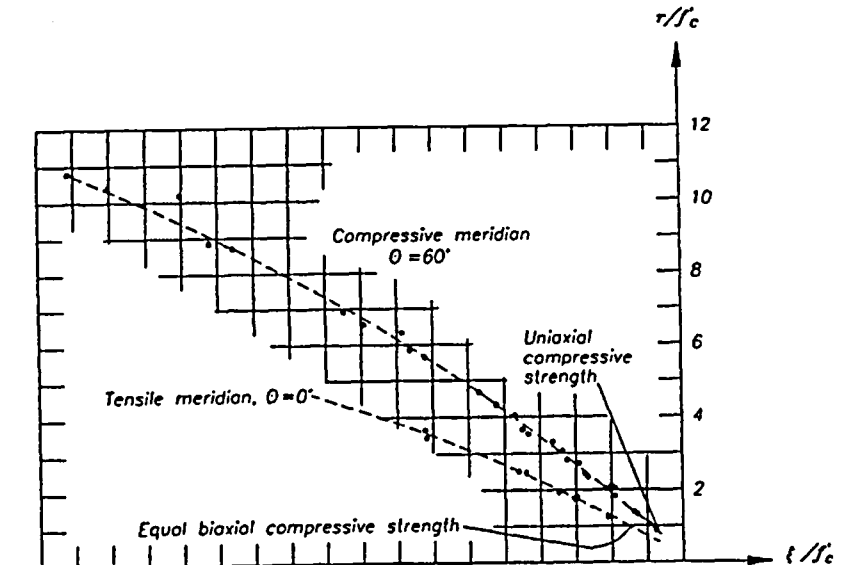

NOTE: $r = \sqrt{2J_2}$
$\xi = I_1/\sqrt{3}$

(c) Typical tensile and compressive meridians.

Fig. 9. Typical failure surface section for concrete from [7]. (a) Deviatoric sections for increasing pressure. (b) Hydrostatic section. (c) Typical tensile and compressive meridians. Note: $r = \sqrt{2J_2}$, $\xi = I_1/\sqrt{3}$.

where $r' = r/r_c$ and $\psi = r_t/r_c$. Note that r' depends only on ψ and θ, and that in general ψ in turn depends on p. For $\theta = 0°$ the formula yields $r' = \psi$ corresponding to pure extension,and for $\theta = 60°$ it yields $r' = 1$ corresponding to pure compression. The value of θ can be obtained from

$$\cos\theta = \frac{\sqrt{3}}{2}\frac{s_1}{\sqrt{J_2}} \quad \text{or} \quad \cos 3\theta = \frac{3\sqrt{3}}{2}\frac{J_3}{J_2^{3/2}},$$

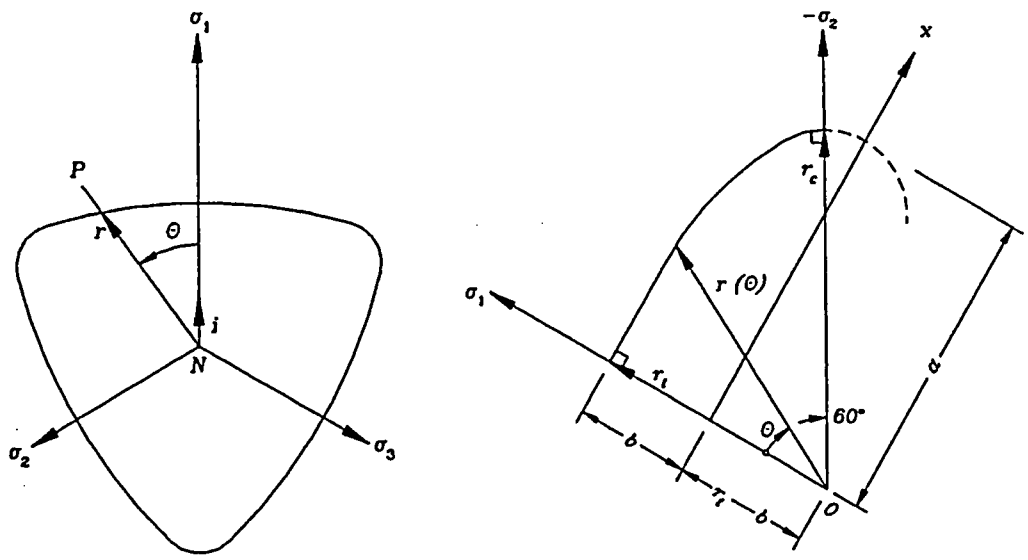

(a) Angle of similarity θ. (b) Elliptical approximation for $0 < \theta < 60$.

Fig. 10. Deviatoric plan section in the Willam Warnke model adapted from [7]. (a) Angle of similarity θ. (b) Elliptical approximation for $0 < \theta < 60$.

where s_1 is the first principal deviatoric stress $= \max \sigma_1 - p, \sigma_2 - p, \sigma_3 - p$, $(\sigma_1, \sigma_2, \sigma_3)$ are the principal stresses, and the stress invariants J_2 and J_3 are given by

$$J_2 = \frac{1}{2}(s_1^2 + s_2^2 + s_3^2), \qquad J_3 = s_1 s_2 s_3 = \begin{vmatrix} s_x & \tau_{xy} & \tau_{xz} \\ \tau_{yx} & s_y & \tau_{yz} \\ \tau_{zx} & \tau_{zy} & s_z \end{vmatrix}.$$

Once the value of r' is known, the original compressive meridians are multiplied by it to obtain the meridian at that location.

Migration between fixed failure surfaces in triaxial extension. Lacking guidance from laboratory data, the transition between fixed failure surfaces in triaxial extension was taken to be the same as in triaxial compression. This transition is given by the λ–η relationship, which has been discussed in the section on damage accumulation. If a different transition were found for the triaxial extension cases, then a second, independent λ–η relationship would have to be implemented.

New compressive meridian. Up to this point in the development it was implied that the compressive meridian is known and input to the code, and the extension meridian can be found as a fraction ψ of the compression one. In fact, depending on data availability, in some pressure ranges it is more appropriate to define the tensile meridian, and then obtain the compressive meridian from the tensile one. The specification built into the new model results from a combination of both approaches, as described here and in the following subsections. For pressures in excess of $f'_c/3$, the input compressive meridian (determined by the parameters a_0, a_1 and a_2 does serve as a basis for all the others. For pressures below $f'_c/3$ and above $-f_t$, we limit the maximum tensile stress on the extension meridian to f_t. This uniquely defines the extension meridian as

$$\Delta\sigma = \frac{3}{2}(p + f_t)$$

which passes through both the triaxial tensile test failure point at $(p, \Delta\sigma) = (-f_t, 0)$and the uniaxial tensile test point at $(p, \Delta\sigma) = (-f_t/3, f_t)$.

At $p = f'_c/3$ we force the two formulations to coincide by determining the appropriate value of ψ. The compressive meridian for pressures less than $f'_c/3$ then follows as the image of the tensile meridian, i.e., the tensile meridian divided by $\psi(p)$ at each pressure p. The following subsections describe the determination of $\psi(p)$ in detail. All three compression failure surfaces (yield, maximum, residual) have corresponding tensile images.

Given this segmental failure surface formulation and the piecewise linear definition of ψ as a function of pressure, the failure surface will not be smooth. This does not violate any fundamental theoretical requirement. In fact, due to the use of a Prandtl–Reuss flow rule as implemented with the "radial return" algorithm, it creates no numerical difficulties either.

Definition of $\psi(p)$. To complete the implementation of the three-invariant failure surface, the function $\psi(p)$ has to be defined for the full range of possible pressures. As mentioned earlier, for concrete, ψ varies from $\frac{1}{2}$ at negative (tensile) pressures to unity at high compressive pressures. In order to satisfy various observations for specific triaxial stress paths, the values of ψ are present within the code for several pressures, as follows.

Case $p \leq 0$ *(tensile pressure).* For $p \leq 0$ the tensile meridian has to include the points $(p, -\Delta\sigma) = (-f_t, 0)$ and $(p, -\Delta\sigma) = (-f_t/3, f_t)$, which represent failure in triaxial and uniaxial tensile tests, respectively. At $p = -2f_t/3$ the compressive meridian is (see Fig. 11)

$$\frac{\Delta\sigma}{\psi} = \frac{3}{2}\left(\frac{-2f_t}{3} + f_t\right)\frac{1}{\psi} = \frac{f_t}{2\psi}.$$

However, this should represent failure in the biaxial tensile test, which test data suggest is approximately given by $\Delta\sigma = f_t$. By equating both stress differences, $\psi = 1/2$ at $p = -2f_t/3$.

Another test of interest is the pure shear test in plane stress. If the coordinates are rotated 45° in plane, the resulting state of stress is $(\sigma_1, \sigma_2, \sigma_3) = (\tau, 0, -\tau)$. Assuming that the maximum tensile stress is limited by f_t, then $\tau = f_t$ at failure. From $(\sigma_1, \sigma_2, \sigma_3)$, $\Delta\sigma$ can be found as:

$$\Delta\sigma = \sqrt{3J_2} = \sqrt{3}f_t.$$

For this test, the principal stress difference is given by r' times the compressive meridian, i.e.

$$\Delta\sigma = r'\frac{3(p + f_t)}{2\psi} = r'\frac{3f_t}{2\psi}$$

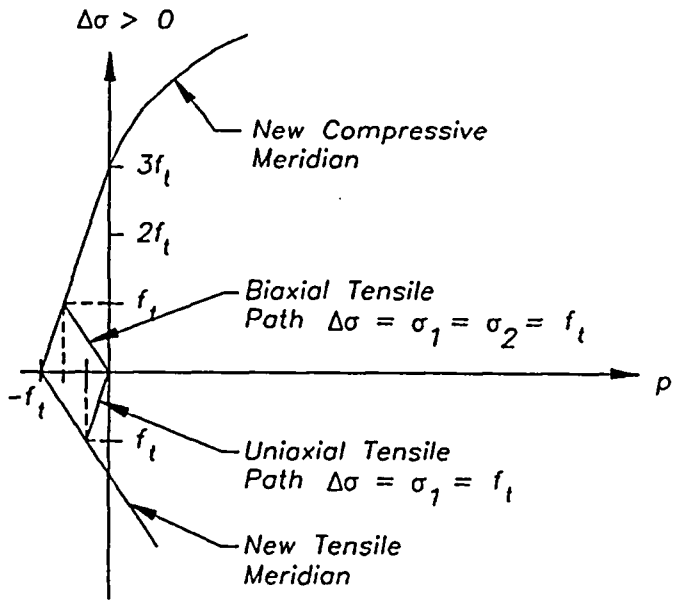

Fig. 11. Derivation of ψ for $p < 0$.

with $r' = r'(\psi, \theta = 30°)$. The two expressions are equal provided $\psi = \frac{1}{2}$ at $p = 0$, because $r'(\frac{1}{2}, 30) = 1/\sqrt{3}$. Thus uniaxial, biaxial, and triaxial tensile failure and pure shear failure can all be plausibly represented with $\psi = \frac{1}{2}$ for $p \leq 0$. For example, this gives the nominal maximum compressive failure surface the form $\Delta\sigma_m = 3(p + f_t)$.

Case $p = f'_c/3$ (*unconfined compression test*). At $p = f'_c/3$, the uniaxial unconfined compressive test yields a principal stress difference of f'_c. The corresponding point on the extension meridian is $\Delta\sigma = \psi f'_c$. This should be limited by the defined extension meridian (Fig. 12)

$$\Delta\sigma = \frac{3}{2}(p + f_t) = \frac{3}{2}\left(\frac{f'_c}{3} + f_t\right)$$

hence

$$\psi = \frac{1}{2} + \frac{3}{2}\frac{f_t}{f'_c}.$$

For example, if $f_t/f'_c = 0.10$ (typical of concretes with $f'_c \leq 5000$ psi) then $\psi = 0.65$. For the WSMR-5 data, and $\psi = 0.606$. Note that this value is actually an upper bound for ψ.

Case $p = 2\alpha f'_c/3$ (*biaxial compression test*). Biaxial compression tests conducted by Kupfer *et al.* [8], have shown failure occurring at $(\sigma_1, \sigma_2, \sigma_3) = (0, \alpha f'_c, \alpha f'_c)$ with $\alpha \approx 1.15$. The stress point lies on the tensile meridian at a pressure $p = 2\alpha f'_c/3 \approx 2.3 f'_c/3$ and a stress difference $|\Delta\sigma_{tm}| = \alpha f'_c$. The corresponding point on the compressive meridian is given in terms of the input parameters as

$$\Delta\sigma_{cm} = a_0 + \frac{p}{a_1 + a_2 p} = a_0 + \frac{2\alpha f'_c/3}{a_1 + a_2(2\alpha f'_c/3)},$$

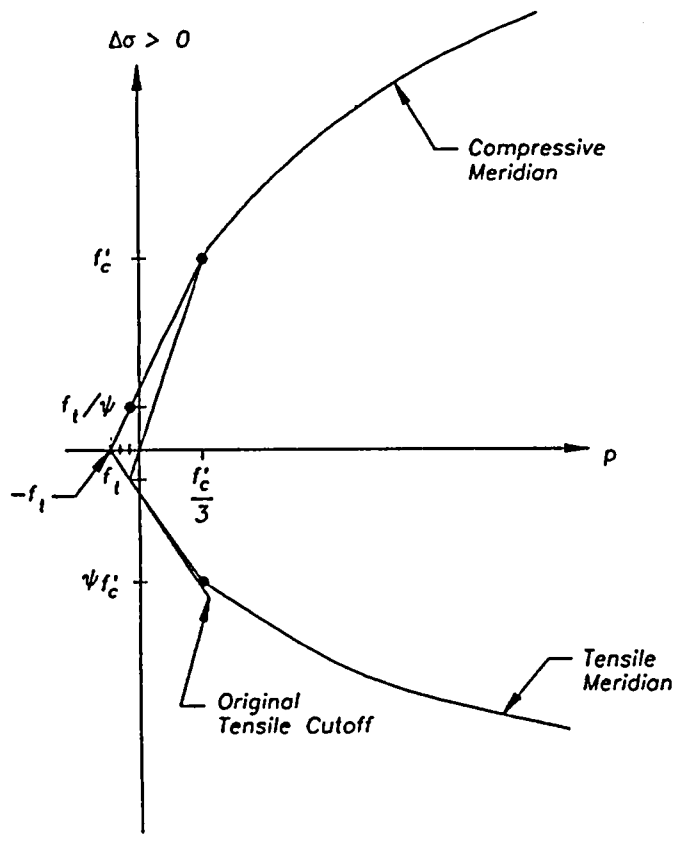

Fig. 12. Cutoff versus new tensile meridian.

so the ratio $\psi = |\Delta\sigma_{tm}/\Delta\sigma_{cm}|$ is

$$\psi = \frac{\alpha f'_c}{a_0 + \dfrac{2\alpha f'_c/3}{a_1 + 2a_2\alpha f'_c/3}} \quad \text{with } \alpha = 1.15.$$

Completion of definition of ψ. For computational purposes, the function $\psi(p)$ is piecewise linear, using, the previously defined values. For higher compression pressures, two additional data points from existing databases were chosen, as follows

$$\psi = \begin{cases} 0.753 & \text{at} \quad p = 3f'_c, \\ 1 & \text{for} \quad p \geq 8.45f'_c. \end{cases}$$

The last entry represents the transition point beyond which the tension and compression meridians are equal, and the failure surface becomes a circle in the deviatoric plane. In summary

$$\psi(p) = \begin{cases} \frac{1}{2}, & p \leq 0, \\ \frac{1}{2} + 3f_t/2f'_c, & p = f'_c/3, \\ \dfrac{\alpha f'_c}{a_0 + \dfrac{2\alpha f'_c/3}{a_1 + 2a_2\alpha f'_c/3}}, & p = 2\alpha f'_c/3, \\ 0.753, & p = 3f'_c, \\ 1, & p \geq 8.45f'_c, \end{cases}$$

and the function is linear between the specified points.

Comparison with previously reported values of ψ. Based on various experimental data, Ahmad and Shah have proposed the following values for ψ [15]:

$$\psi = \begin{cases} 0.686 & \text{for } \frac{1}{3} \leq p/f'_c < 1.75, \\ 0.610 + 0.0435(p/f'_c) & \text{for } 1.75 \leq p/f'_c < 8.9. \end{cases}$$

The proposed values of ψ for $p/f'_c \geq 3$ are based on this and additional data [6]. For $p/f'_c = \frac{1}{3}$, using $\psi = 0.686$ implies that, in some cases and while unloading uniaxially from an isotropic compression state, the failure surface would only be reached for $\sigma_1 = 0.124f'_c$. This would probably only happen for concretes with low compressive strengths ($f'_c \leq 4000$ psi), where $f_t/f'_c \geq 0.10$.

Based on several data sets, Chen [7] suggests that

$$\psi = \begin{cases} 0.5 & \text{for } p/f'_c \approx 0, \\ 0.8 & \text{for } p/f'_c \approx 7. \end{cases}$$

Radial rate enhancement

Since in typical experiments rate enhancements are obtained along radial paths from the origin in the principal stress difference versus pressure plane (via unconfined compressive and tensile tests), strength enhancement was implemented in general along radial stress paths. This is accomplished as follows (see Fig. 13). Let r_f be the enhancement factor and p the pressure after calling the equation of state subroutine. The enhanced value $\Delta\sigma_e$ of the failure surface at pressure p is desired, assuming the enhancement factor is applied radially. To get $\Delta\sigma_e$ an "unenhanced" pressure p/r_f is first obtained, then the unenhanced strength $\Delta\sigma(p/r_f)$ is calculated for the specified failure surface. Finally, the unenhanced strength is multiplied by the enhancement factor to give

$$\Delta\sigma_e = r_f\Delta\sigma(p/r_f).$$

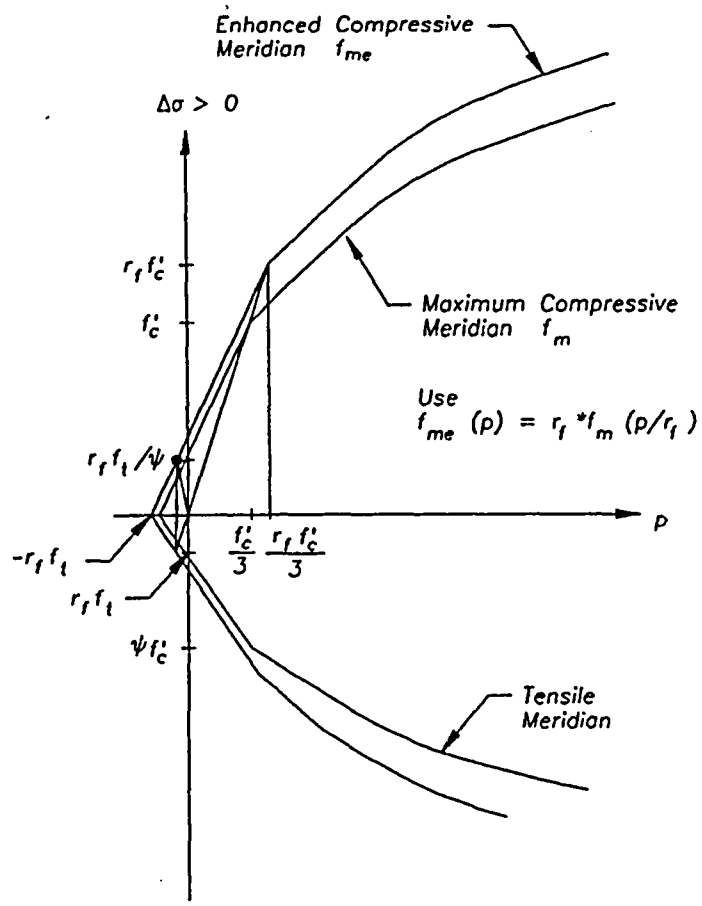

Fig. 13. New rate enhancement in tension and compression.

This formulation presents the following advantages:

- The code input is obtained directly from the test data at the same strain rate;
- Strength is equally enhanced along any radial stress path, including uniaxial, biaxial and triaxial tension, and uniaxial and biaxial compression — this is far more consistent with data than the earlier formulation;
- Different rate enhancements can be included in tension and compression by linking the enhancement factor itself to pressure;
- The method was very simple to implement in the code.

Compressive meridian in the softening regime

Compressive meridian for negative pressures. With the modifications discussed so far, if $p < 0$ and softening is underway, there will be a vertical segment in the current failure surface (in the p versus $\Delta\sigma$ plane, see Fig. 14) due to the reduction in minimum pressure p_c. In other words, the current failure surface is given by:

$$\Delta\sigma = \eta(\Delta\sigma_m - \Delta\sigma_r) + \Delta\sigma_r \quad \text{for } p > p_c$$

and a vertical segment at $p = p_c$.

To avoid this vertical segment but maintain the reduction in magnitude of p_c, a modified maximum failure surface $\Upsilon_1(p,\eta)$ can be defined as follows when pressure is negative and softening is under way ($\lambda > \lambda_m$):

$$\Upsilon_1(p,\eta) = \Upsilon_m(p) - \frac{p_f - p}{p_c - p_c(\eta)}\Upsilon_m(p_c) = 3\left(\frac{p}{\eta} + f_t\right),$$

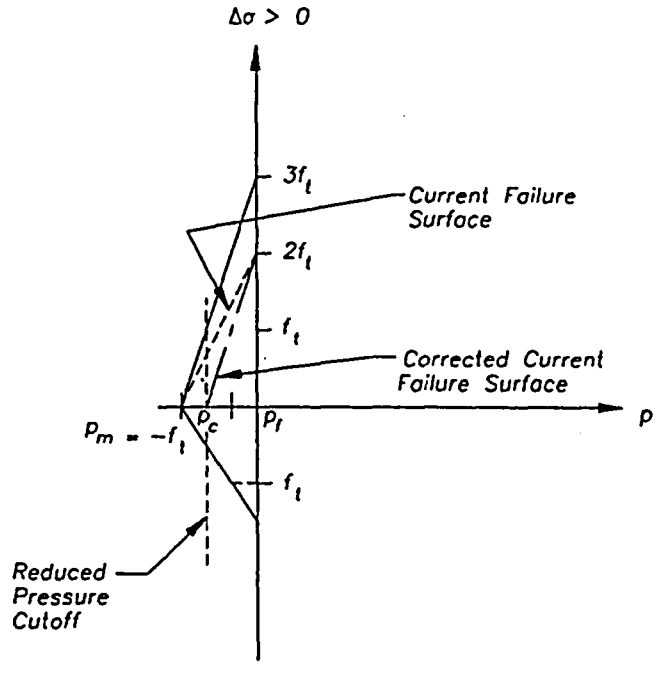

Fig. 14. Failure surface evolution during tensile strain softening.

where Υ_m is the nominal maximum failure surface in compression $= 3(p + f_t)$, p_f the intersection of the residual surface with the pressure axis $= 0$ (for concrete), $p_c(\eta)$ is $\eta p_m + (1 - \eta)p_f = \eta p_m$, and p_m the intersection of the maximum surface with the pressure axis $= -f_t$.

As defined, Υ_1 is continuous with Υ_m at $p = p_f = 0$. The current failure surface in the softening range can then be defined as follows:

$$\Upsilon(p,\eta) = \begin{cases} \eta\Delta\sigma_m(p) + (1-\eta)\Delta\sigma_f(p), & p > p_f, \\ \eta\Upsilon_1(p,\eta) = \eta\Upsilon_m - \dfrac{p_f - p}{p_f - p_m}\Upsilon_m(p_c) = 3(p + \eta f_t), & p \le p_f. \end{cases}$$

The formula above is uncorrected for rate enhancement. The correction follows as outlined in the section on radial rate enhancement. Given an updated pressure p (which implicitly includes effects of rate enhancement), the corresponding "unenhanced" state is denoted by $p_u = p/r_f$, where r_f is the enhancement factor. The current unenhanced failure surface for negative pressures can be written as

$$\Upsilon_u(p_u,\eta) = \eta\Upsilon_1\left(\frac{p}{r_f},\eta\right) = 3\left(\frac{p}{r_f} + \eta f_t\right) \quad \text{for } \frac{p}{r_f} < p_f \quad (p_f = 0 \text{ for concrete}).$$

The corresponding enhanced failure surface follows by multiplying by r_f:

$$\Upsilon_e(p,\eta) = r_f\left[\eta\Upsilon_m\left(\frac{p}{r_f}\right) - \frac{p_f - p/r_f}{p_f - p_m}\Upsilon_m(p_c)\right] = 3(p + \eta r_f f_t).$$

This is the expression to use in the formulas for stress and damage update to be derived in the next subsection. The corresponding partial derivative with respect to η for $p < p_f$ is

$$\Upsilon_\eta = \frac{\partial\Upsilon}{\partial\eta} = r_f\left[\Upsilon_m\left(\frac{p}{r_f}\right) + \left(p_f - \frac{p}{r_f}\right)\Upsilon'_m(p_c)\right] = 3r_f f_t.$$

Corrections to the flow rule. The foregoing modification has the undesirable effect of complicating the dependence of the failure surface on p and η. The expressions for the updated stresses and the increment $d\lambda$ of the damage parameter must also be modified. The derivation, which is based on the assumption of Prandtl-Reuss (volume-preserving) plastic flow, is presented below.

In matrix symbolic notation, the decomposition of strain increments into elastic and plastic parts is

$$d\varepsilon = d\varepsilon^p + d\varepsilon^e = \sigma' d\mu + C d\sigma,$$

where σ' is the deviatoric stress and C the elastic tensor. Premultiplying by C^{-1}

$$C^{-1} d\varepsilon = C^{-1}\sigma' d\mu + d\sigma$$

and by $\nabla_\sigma f$, the gradient with respect to stress of the failure function $f = \sqrt{3J_2} - \Upsilon[\sigma, \eta(\lambda)]$,

$$\nabla_\sigma f C^{-1} d\varepsilon = \nabla_\sigma f C^{-1}\sigma' d\mu + \nabla_\sigma f d\sigma.$$

But by differentiating the consistency equation $f(\sigma, \int d\lambda) = 0$ (which ensures that the stress point remains on the failure surface during plastic flow), we have

$$\nabla_\sigma f d\sigma = f_{,\lambda} d\lambda = 0 \Rightarrow \nabla_\sigma f d\sigma = -f_{,\lambda} d\lambda,$$

where the comma denotes a partial derivative. Therefore

$$\nabla_\sigma f C^{-1} d\varepsilon = \nabla_\sigma f C^{-1}\sigma' d\mu - f_{,\lambda} d\lambda.$$

On the other hand, by definition

$$d\lambda = h(\sigma) d\bar{\varepsilon}^p = h(\sigma)\sqrt{(2/3) d\varepsilon_{ij}^p d\varepsilon_{ij}^p} = h(\sigma)\sqrt{(2/3)\sigma' : \sigma'}\, d\mu = h(\sigma)(2/3)\sqrt{3J_2}\, d\mu,$$

where in this model $h(\sigma) = (1 + p/r_t f_t)^{-b^2}/r_t$ when $p < 0$. By substituting $d\lambda$ and solving for $d\mu$,

$$d\mu = \frac{\nabla_\sigma f C^{-1} d\varepsilon}{\nabla_\sigma f C^{-1}\sigma' - (2/3) f_{,\lambda} h(\sigma)\sqrt{3J_2}}.$$

Now note that $C^{-1} d\varepsilon = d\sigma^* =$ trial elastic stress increment, $C^{-1}\sigma' = 2G\sigma'$, and with some manipulation it can be shown that

$$(\nabla_\sigma f)\sigma' = \frac{3\sigma'_{ij}}{2\sqrt{3J_2}}\sigma'_{ij} = \sqrt{3J_2},$$

so

$$d\mu = \frac{\nabla_\sigma f d\sigma^*}{2G\sqrt{3J_2} - (2/3) f_{,\lambda} h(\sigma)\sqrt{3J_2}}.$$

At any time step the failure surface will change due to changes in both presence and η. The pressure change is known just after entering the material model subroutine. If Y^* denotes the failure surface corresponding to the updated pressure but the prior value of η, and Y_{n+1} the fully updated surface, the increment due to η will be

$$\begin{aligned}\Upsilon_{n+1} - \Upsilon^* &= \frac{\partial \Upsilon}{\partial \eta} d\eta = \frac{\partial \Upsilon}{\partial \eta}\frac{d\eta}{d\lambda} d\lambda = \frac{\partial \Upsilon}{\partial \eta}\frac{d\eta}{d\lambda} h(\sigma) d\bar{\varepsilon}^p \\ &= \frac{\partial \Upsilon}{\partial \eta}\frac{d\eta}{d\lambda} h(\sigma)(2/3)\sqrt{3J_2}\, d\mu \\ &= \Upsilon_{,\eta}\eta'(\lambda) h(\sigma)(2/3)\frac{\nabla_\sigma f d\sigma^*}{2G - (2/3) f_{,\lambda} h(\sigma)}.\end{aligned}$$

Now because $f(\sigma_n) = 0$, $f(\sigma^*) = f(\sigma_n + d\sigma^*) = (\nabla_\sigma f)\,d\sigma^*$. But by definition, $f(\sigma^*) = \sqrt{3J_2^*} - \Upsilon^*$. Furthermore, since $f(\sigma, \lambda) = \sqrt{3J_2} - \Upsilon(p, \eta)$, $f_{,\lambda} = -\Upsilon_{,\eta}\eta'(\lambda)$. Therefore the update to the failure surface (after the trial elastic part) is

$$\Upsilon_{n+1} - \Upsilon^* = \frac{\Upsilon_{,\eta}\eta'(\lambda)h(\sigma)}{3G} \frac{f(\sigma^*)}{1 + \Upsilon_{,\eta}\eta'(\lambda)h(\sigma)/3G},$$

where

$$\Upsilon_{,\eta} \begin{cases} r_f[\Delta\sigma_m(p/r_f) - \Delta\sigma_f(p - r_f)], & p \geq p_f, \\ 3r_f f_t, & p < p_f. \end{cases}$$

For the update of λ, the increment is

$$d\lambda = h(\sigma)\,d\bar{\varepsilon}^p = h(\sigma)\frac{2}{3}\sqrt{J_2}\,d\mu = \frac{h(\sigma)[\sqrt{3J_2^*} - \Upsilon(p^*, \eta_n)]}{3G\left[1 + \dfrac{\Upsilon_{,\eta}\eta'(\lambda)h(\sigma)}{3G}\right]}.$$

Shear modulus correction

With the constant Poisson's ratio option and equation of state 8, the original model 16 computes the elastic shear modulus from the specified constant Poisson's ratio and the current *unload/reload* bulk modulus. This can easily lead to a negative effective Poisson's ratio on loading whenever there is a large enough disparity between loading and unload/reload bulk moduli. In a first attempt at correcting this deficiency, the shear modulus was made dependent on whichever bulk modulus was currently in effect. However, this method failed because even infinitesimal pressure oscillations, e.g. during an unconfined compressive loading, led to large shear modulus oscillations which did not reflect the nominally continuously increasing load. In addition, these oscillations were encouraged by the fact that elastic energy could be generated whenever pressure increased while shear stress decreased.

A better approach is to compute the shear modulus based on a scaled bulk modulus, one which varies from the loading to the unload/reload value depending on how far the pressure is below the virgin curve. A scaling factor which varies from zero to unity as pressure drops from the virgin loading curve to p_f is given by

$$\varphi = \frac{-\Delta\varepsilon}{-\Delta\varepsilon + (p - p_f)/K_u},$$

where $\Delta\varepsilon = \varepsilon_{v,\min} - \varepsilon_v$, ε_v is volumetric strain, and K_u is the unload/reload bulk modulus from equation of state 8. If K_L is the corresponding loading modulus, the scaled bulk modulus is

$$K' = (K_L - K_U)e^{-5.55\varphi} + K_U,$$

where the constant 5.55 is chosen so that K' will increase half way to the unload/reload value when p has dropped 1/8 of the way from the virgin curve to p_f. The shear modulus is then calculated as

$$G = (1.5 - 3\nu)K'/(1 + \nu).$$

APPLICATION EXAMPLE: SUBSTANTIAL DIVIDING WALLS

Substantial dividing walls (SDWs) in munitions production, maintenance, and storage facilities are used to subdivide explosives to prevent sympathetic detonation and to provide operational shields for personnel. They are 12-in. thick concrete walls with #4 reinforcing bars at 12-in. spacings on each face and in each direction, and without any shear reinforcing. Current Army and Air Force safety regulations assume that the 12-in. SDW's will prevent

propagation for up to 425 pounds of Class/Division 1.1 explosives. This study seeks to provide a verification of the propagation prevention limits of the 12-inch SDW [16].

Although both the mass and velocity of secondary fragments are used for their capability of detonating the acceptor charge, this study was tasked exclusively with estimating their velocity. This is due to the wide variation in fragment sizes and the difficulty for current analytical model to provide reliable estimates of fragment sizes. Established criteria indicates expected maximum fragment velocities close to 500 feet per second for typical fragment sizes.

Load definition

Definition of airblast loading was performed with two widely used codes: SHOCK [17] to produce the shock loading (early time airblast) resulting from the incident blast wave and FRANG [18] to compute the gas pressure (late time airblast) resulting from expansion of the detonation products and heating of the air within the room. The process adopted was to compute loads independently of the response of the wall, i.e. the walls were assumed to be rigid. However, the assumption of rigid boundary conditions is considered reasonable for this set of problems because the shock pressure pulse (which typically dominates gas pressures) lasts less than a millisecond, in which time the wall has not yet had time to move significantly so that interaction might take place.

One potentially significant effect of the loading produced by realistic munitions which was not considered in this study is that associated with the primary fragments. The primary fragments, produced by the breaking up of a weapon's casing upon detonation, will impact the wall and may provide a sizable additional source of impulse and possibly cause significant degradation of the wall's components (e.g. abrasion of cover concrete, cutting of front face rebar) [19]. In this paper light casing donors are considered. The resultant combined loading used is shown in Fig. 15.

Test description

A description of the selected test (C-6) and relevant design data was obtained from [20]. This experiment was conducted in the early 1960s at the Naval Ordnance Test Station (NOTS) in China Lake, California, and consisted of a cased donor munition placed in a cubicle with three sides walls (no roof) with numerous acceptor charges placed immediately outside the dividing walls, as shown in Fig. 16. The 272-lb charge was detonated, resulting in complete destruction of the dividing walls but no sympathetic detonations. Fragments velocities of about 500 ft/s were measured [20].

Structural model

The SDWs analyzed were components of a cell where munitions are manufactured, stored, or handled. Two typical configurations for these cells were analyzed; one with two

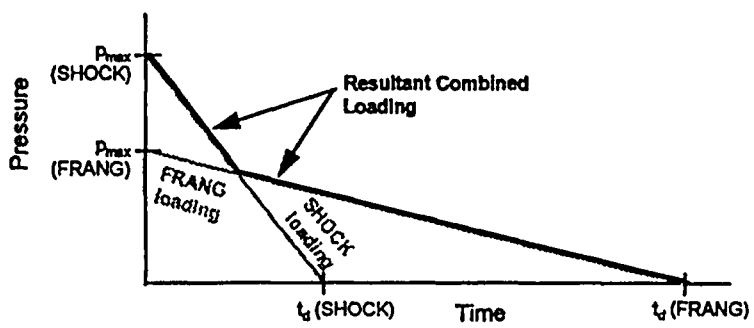

Fig. 15. Method used to combine gas and blast pressure loadings.

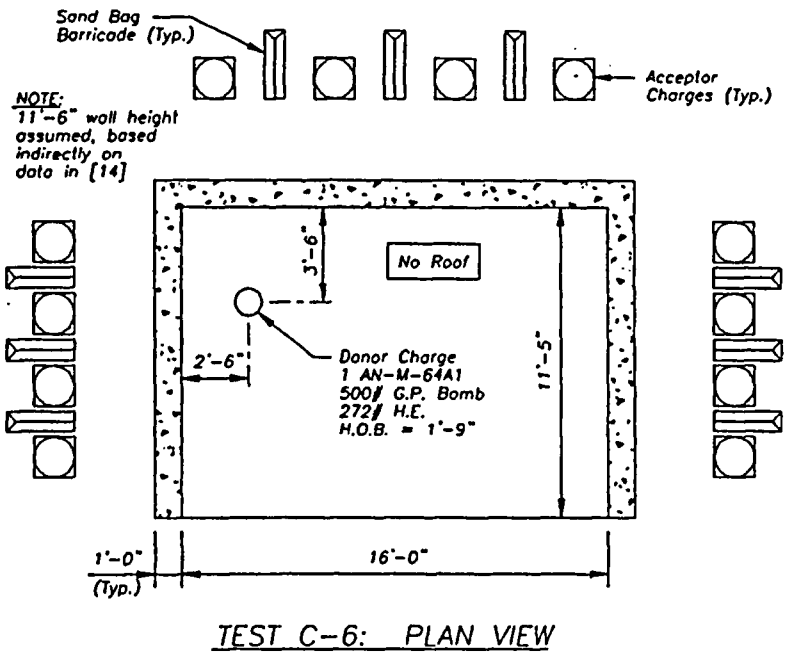

Fig. 16. Test C-6.

frangible walls (roof and side wall) and one with only one (side wall only). The discretization used to represent a typical SDW in the parametric calculations is shown in Fig. 17, which illustrates a model with three supported sides (one side wall is frangible). The model for a wall with two supported sides (roof is also frangible) is similar, except that the stub along the roof line is omitted. The following model features are noteworthy:

1. The selected mesh has six brick elements through the thickness for the concrete, one for the cover on each side and four inside the rebar cage; the thickness of cover is taken at $1\frac{1}{2}$ in., plus one bar diameter (centerline of the two-way mesh). The elements are approximately 2 in. cubes.
2. Reinforcing steel was modeled discretely using truss elements at 12-in. spacings in each direction (in this example, using beam elements provided a small improvement in the results, but truss elements reduced the computational time).
3. Stubs of the floor, side wall, and, where present, roof were included in the model with fixed boundary conditions applied at the end of each stub; the stubs were one thickness in length.

The material model used for steel, identified in DYNA3D as Material 19, has similar features as the concrete model: inclusion of strain rate effects, nonlinear post-yield hardening, and failure upon reaching a predefined level of strain. This material model was modified to support truss and beam elements [21]. Bar failure is an essential property as bar failure is observed in each one of the runs performed in this study, and without accurate representation of the breakage of reinforcing bars, the resulting secondary fragment velocity could not be adequately predicted. An example of the stress strain curves required as input for this material is presented in Fig. 18: one for static properties (49 ksi yield stress, 81 ksi ultimate), one for infinite rate (limit case with 88 ksi yield stress, 97 ksi ultimate), and one for an intermediate value at which properties have been measured (72 ksi yield stress, 91 ksi ultimate at 1 s^{-1}). This allows independent scaling of yield and ultimate strengths as a function of strain rate. The failure strain was 12% (Fig. 18).

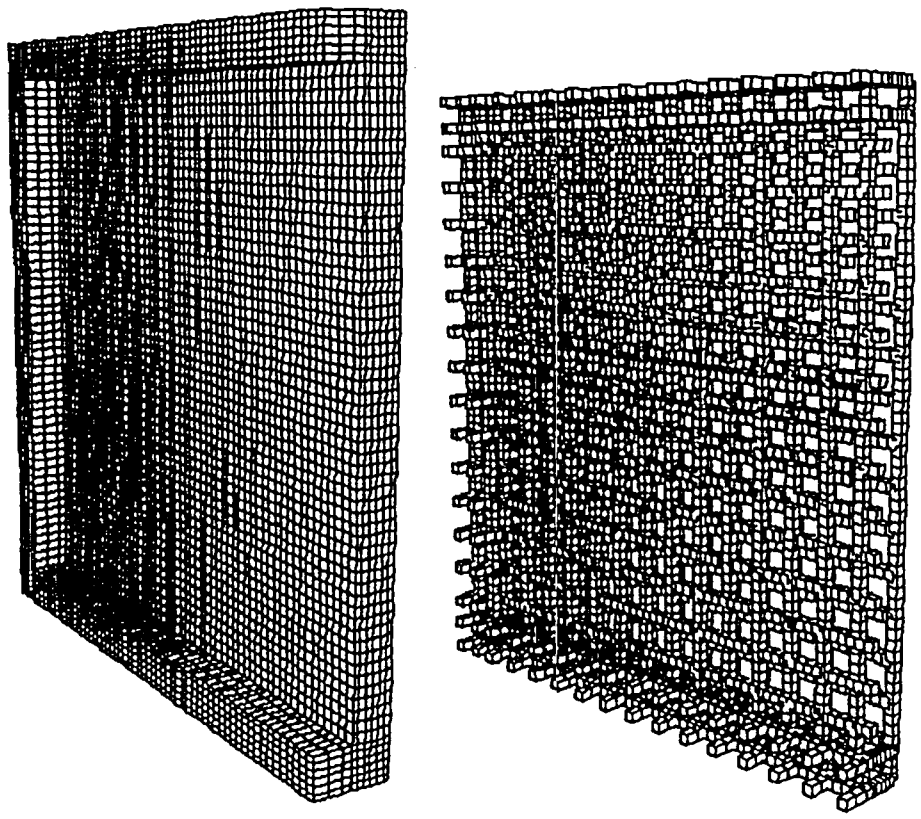

Fig. 17. View of DYNA3D concrete and steel meshes (3-sided support).

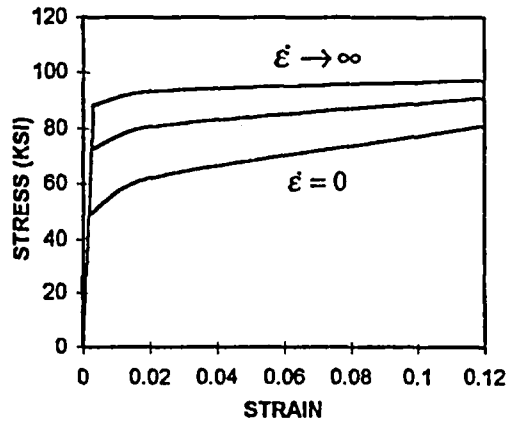

Fig. 18. Inputs to material 19 (steel).

Comparison of analytical and test results for test C-6

The analysis was performed with both the original and new material models. Both runs indicated a similar type of breaching failure in the immediate area of the charge, with shear failure along the floor and side wall (Fig. 19). However, with the original model, it can first be observed that the elements along the edges distort significantly: this is due to the brittle nature of this model in uniaxial tension [as shown in Fig. 6(a)]. In contrast the new model results in small deformations along the same edges. Also the original model locks up in biaxial tension [as well as triaxial hydrostatic tension—see Fig. 6(b)] where the stress

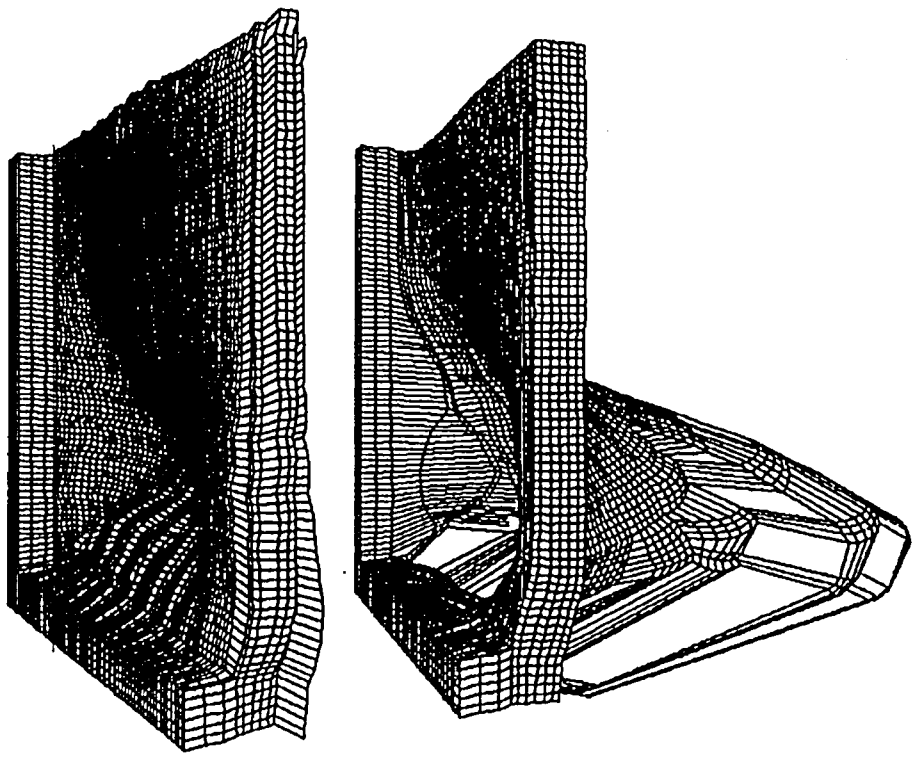

(a) Original version. (b) Current version

Fig. 19. Comparison of wall deformations using different versions of the concrete material model. (a) Original version. (b) Current version.

reaches $f_t/2$ ($f_t/3$ in triaxial tension) and remains there upon further straining. This results in excessive energy dissipation in biaxial tension, and significantly reduced deformations at the center of the wall, as shown in Fig. 19(a). Figure 19(b) shows that the new model properly represents the observed breaching.

Calculated secondary fragment velocities are presented in Fig. 20. The figure shows the velocity of a node on the front face of the slab where the velocity is in the direction normal to the slab's surface; the node is located approximately 1 ft above the intersection of the dividing wall with the floor, in line with the charge. This represents the location where maximum velocity was observed in the finite element model. The velocity time histories indicate that for both models fragment velocities initially reach about 430 ft/s, then the original model shows a significant and unexpected velocity reduction, probably due to the excessive energy dissipation in biaxial tension.

The calculations using the new model predicted fragment velocities of up to 470 ft/s which compare well with the observed 500 ft/s. Upon failure the velocity remains constant, indicating complete separation of the debris. In conclusion, the test results appear to confirm the validity of the new material model, both with regard to the predicted secondary fragment velocity, as well as the level and mode of damage incurred by the dividing wall.

CONCLUSIONS

The concrete material model in DYNA3D has been significantly modified to properly represent material behavior along multiple radial paths in the $\Delta\sigma$ versus p space, including uniaxial, biaxial and triaxial tension and compression. The plasticity model has been extended to replace the tensile cutoff and provide a smooth transition to the residual failure

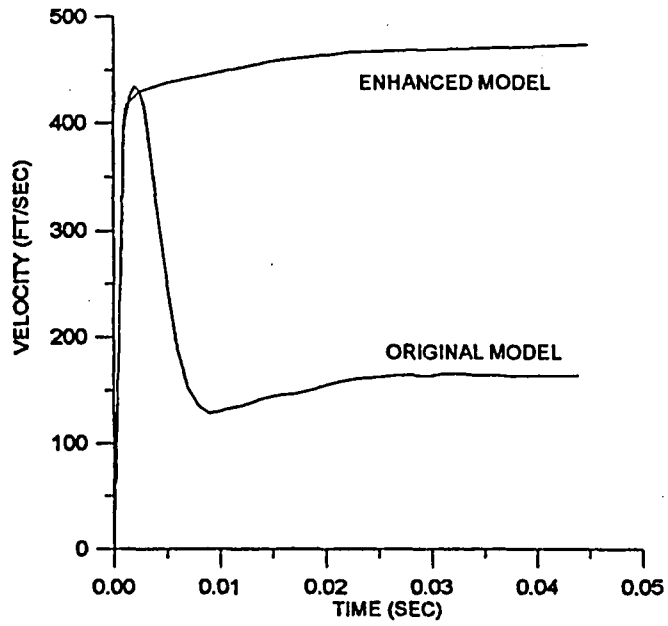

Fig. 20. Velocity time histories.

surface. A new algorithm captures strain rate effects properly in any radial path. The model has shown to properly represent the blast response of Substantial Dividing Walls subjected to standard charges.

REFERENCES

1. R. G. Whirley and J. O. Hallquist, *DYNA3D: A Nonlinear Explicit Three-Dimensional Finite Element Code for Solid and Structural Mechanics, User Manual*, Report UCRL-MA-107254, Lawrence Livermore National Laboratory, Livermore, CA, 1991.
2. Task Committee on Finite Element Analysis of Reinforced Concrete Structures, Structural Division Committee on Concrete and Masonry Structures, *Finite Element Analysis of Reinforced Concrete*, State-of-the-Art Report, American Society of Civil Engineers, 1982.
3. ASCE–ACI Joint Committee 447 on Finite Element Analysis of Reinforced Concrete Structures, *Finite Element Analysis of Reinforced Concrete* II, State-of-the-Art Report, *Proc. Int. Workshop*, American Society of Civil Engineers, 1991.
4. J. A. Zukas, *High Velocity Impact Dynamics*. Wiley, New York, 1990.
5. T.A. Shugar, T. J. Holland and L. J. Malvar, Applications of finite element technology to reinforced concrete explosive containment structures, *Proc. 25th DoD Explosive Safety Seminar*, Anaheim, CA, 1992.
6. S. Joy and R. Moxley, *Material Characterization, WSMR-5 3/4-inch Concrete*, Report to the Defense Special Weapons Agency, USAE Waterways Experiment Station, Vicksburg, MS, 1993 (limited distribution).
7. W.F. Chen, *Plasticity in Reinforced Concrete*, McGraw Hill, New York, 1982.
8. H. Kupfer, H. Hilsdorf and H. Rush, Behavior of concrete under biaxial stresses, *ACI J.* 66, 656–666 (1969).
9. Comité Européen du Béton—Fédération Internationale de la Précontrainte, *CEB-FIP Model Code 90*, Thomas Telford Services, London, 1993.
10. L. J. Malvar, J. E. Crawford, J. W. Wesevich and B. Dunn, *Modifications to DYNA3D Material Model 16*, Report No. TM-93-13 to the Defense Special Weapons Agency, Appendix B, Karagozian and Case, Glendale, CA, 1993.
11. L. J. Malvar, J. E. Crawford and J. W. Wesevich, *A New Concrete Material Model for DYNA3D*, Report TM 94-14 to the Defense Nuclear Agency, Karagozian and Case, CA, 1994.
12. Z. P. Bazant, (Ed.), *Fracture Mechanics of Concrete Structures, State-of-the-art and Proc. 1st Int. Conf. (FraMCos I)* Breckenridge, CO, 1992, Elsevier Applied Science, Amsterdam (xxx).
13. J. Oliver, A consistent characteristic length for smeared cracking models, *Int. J. Numer. Meth. Engng.* 28, p. 461 (1989).
14. J.G. Rots, Computational Modeling of Concrete Fracture, Ph.D. Dissertation, Delft University of Technology, Delft, The Netherlands, 1988.

15. S. H. Ahmad and S. P. Shah, Complete triaxial stress–strain curves for concrete, *J. Structural Division, ASCE* **108** (ST4), p. 728(1982).
16. D. Bogosian, *Parametric Analysis of 12-in. Substantial Dividing Walls*, Report No. TM-94-20, Karagozian and Case, CA, 1994.
17. *SHOCK User's Manual*, Version 1.0, Naval Civil Engineering Laboratory, Port Hueneme, CA, 1988.
18. *FRANG User's Manual*, Naval Civil Engineering Laboratory, Port Hueneme, CA, 1989.
19. L. J. Malvar, J. W. Wesevich, Evaluation of numerical techniques for inclusion of material degradation from bomb casing fragments, *65th Shock and Vibration Symp.*, San Diego, CA, October 1994.
20. A. Schwartz, *Report on Summary and Analysis of Full Scale Dividing Wall Test and Comparisons with Analytically Predicted Results*, Picatinny Arsenal, Dover, NJ, 1964.
21. D. Pelessone, Charman, C, User's Manual Supplement for DNA Version of the DYNA3D Code, GA-C20983, Project No. 3830, General Atomics, 1992.